ACS NANO

www.acsnano.org

Polyelemental Nanoparticles as Catalysts for a Li−O_2 Battery

Woo-Bin Jung, Hyunsoo Park, Ji-Soo Jang, Do Youb Kim, Dong Wook Kim, Eunsoo Lim, Ju Ye Kim, Sungho Choi, Jungdon Suk, Yongku Kang, Il-Doo Kim, Jihan Kim, Mihye Wu,* and Hee-Tae Jung*

Cite This: *ACS Nano* 2021, 15, 4235−4244

Read Online

ACCESS | Metrics & More | Article Recommendations | Supporting Information

ABSTRACT: **The development of highly efficient catalysts in the cathodes of rechargeable Li−O_2 batteries is a considerable challenge. Polyelemental catalysts consisting of two or more kinds of hybridized catalysts are particularly interesting because the combination of the electrochemical properties of each catalyst component can significantly facilitate oxygen evolution and oxygen reduction reactions. Despite the recent advances that have been made in this field, the number of elements in the catalysts has been largely limited to two metals. In this study, we demonstrate the electrochemical behavior of Li−O_2 batteries containing a wide range of catalytic element combinations. Fourteen different combinations with single, binary, ternary, and quaternary combinations of Pt, Pd, Au, and Ru were prepared on carbon nanofibers (CNFs) via a joule heating route. Importantly, the Li−O_2 battery performance could be significantly improved when using a polyelemental catalyst with four elements. The cathode containing quaternary nanoparticles (Pt−Pd−Au−Ru) exhibited a reduced overpotential (0.45 V) and a high discharge capacity based on total cathode weight at 9130 mAh g^{-1}, which was ∼3 times higher than that of the pristine CNF electrode. This superior electrochemical performance is be attributed to an increased catalytic activity associated with an enhanced O_2 adsorbability by the quaternary nanoparticles.**

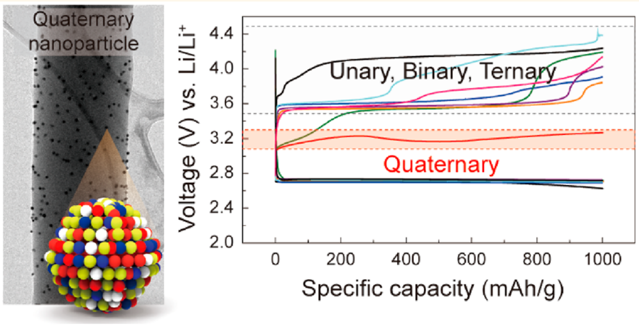

KEYWORDS: *polyelemental nanoparticle, noble metals, joule heating, Li−O_2 batteries, catalyst*

Because of the growing demand for high-energy-density devices, the rechargeable Li−O_2 battery with high energy density of ∼3500 Wh kg^{-1} has been intensively investigated to meet these energy requirements.[1] The oxygen reduction reaction (ORR) occurs during discharge on the cathode, when lithium and oxygen react to form lithium peroxide (Li_2O_2) as a discharge product. The oxygen evolution reaction (OER) occurs during charging, when Li_2O_2 is electrochemically decomposed into lithium and oxygen ($2Li^+ + O_2 + 2e^- \rightleftarrows Li_2O_2$, 2.96 V).[2−5] Critical challenges associated with Li−O_2 battery development are mostly related to the slow formation and decomposition kinetics of Li_2O_2 during cycling. Many studies have been conducted to investigate ways to overcome the sluggish kinetics of ORR and OER, primarily through the incorporation of catalysts in the cathode, which can reduce discharge and charge overpotential.[6−9]

To date, platinum (Pt), palladium (Pd), gold (Au), and ruthenium (Ru) have been the most frequently used catalysts because of their excellent catalytic activity in both ORR and OER.[7,10,11] The increased O_2 binding energy on noble-metal catalysts can facilitate the second electron transfer, which is necessary for Li_2O_2 formation. Additionally, catalyzing Li_2O_2 decomposition can lower the OER activation barrier and enable rapid O_2 diffusion by exposing the cathode surface without blocking the pores. Recently, multicomponent catalysts, such as Pt−Au,[12] Pt−Ir,[13] Pt−Co,[14] and Pd−Fe,[15] have attracted much attention for further improving catalytic activity. Li−O_2 cell performance with multicomponent noble-metal catalysts can be significantly improved due to synergistic catalytic effect of polyelemental nanoparticles in comparisoin with Li−O_2 batteries with single-metal catalysts. Changes in the adsorption strength between the catalyst and discharge products as well as the increased number of active sites in multicomponent catalysts can enhance the electrochemical performance of Li−O_2 batteries. However, although noble metal hybrids have been shown to enhance Li−O_2 battery

Received: August 4, 2020
Accepted: March 3, 2021
Published: March 11, 2021

https://doi.org/10.1021/acsnano.0c06528

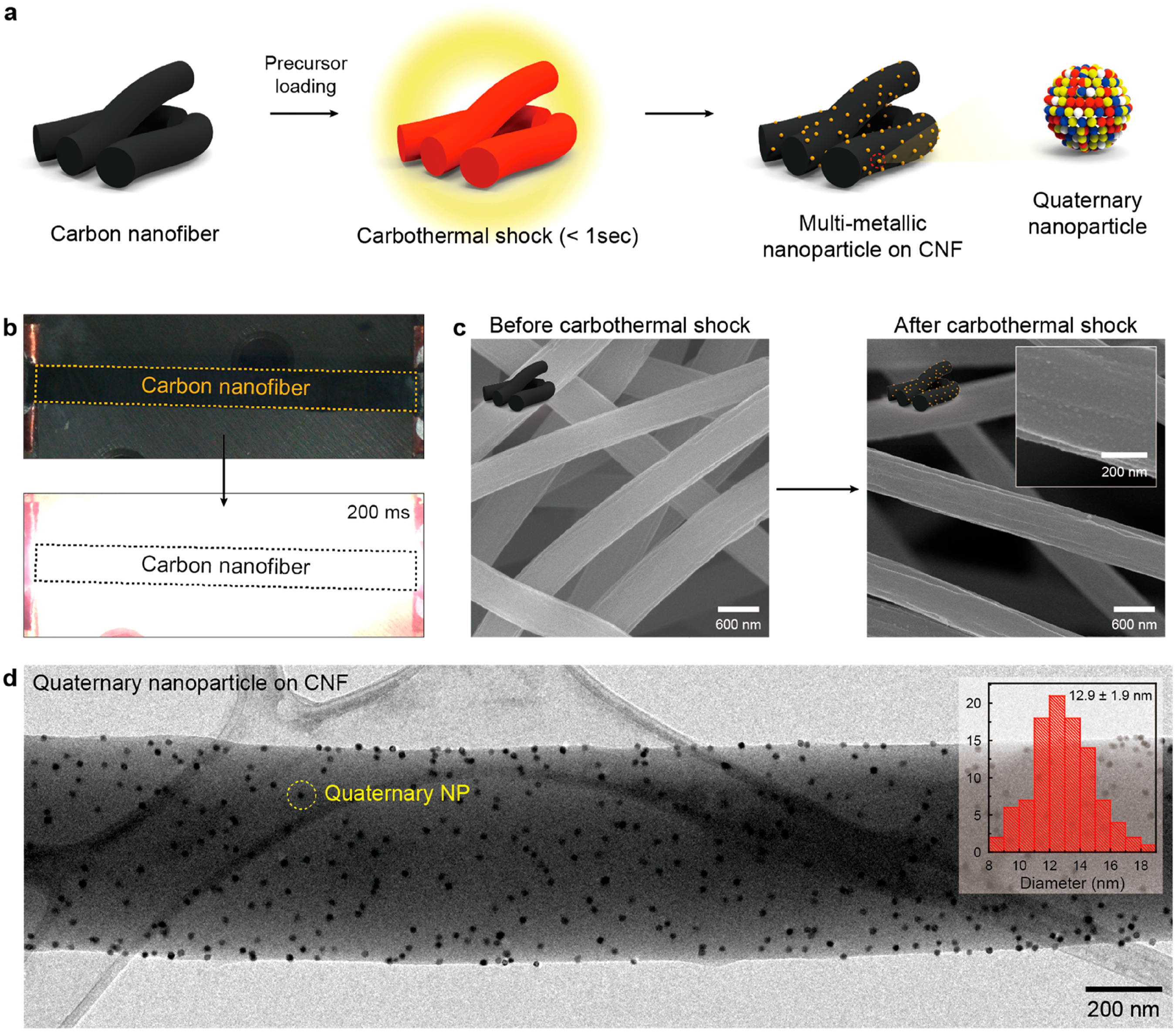

Figure 1. Thermal shock for synthesis of quaternary nanoparticle on carbon nanofiber. (a) Schematic drawing of thermal shock method. (b) Bright light of carbon nanofiber during thermal shock. (c) SEM images of carbon nanofiber before and after thermal shock. (d) Well-dispersed quaternary nanoparticles on the carbon nanofiber with ∼13 nm size.

performance, previous works have been limited to combinations of two metal elements. Here, we report a wide range of polyelemental catalysts with single, binary, ternary, and quaternary combinations of Pt, Pd, Au, and Ru in the cathode of Li−O_2 batteries. In this work, we demonstrate that the electrochemical performance of Li−O_2 cells assembled on carbon nanofibers' (CNFs) support is strongly influenced by the number of multielements anchored on the surface of CNFs and their combinations. This study enables the research of screening the combination of components optimized for the Li−O_2 battery catalyst by a high throughput process.

RESULTS AND DISCUSSIONS

Fourteen different combinations of polyelemental catalysts with single, binary, ternary, and quaternary combinations of Pt, Pd, Au, and Ru nanoparticles were prepared on CNFs by carbothermal shock heating (Joule heating) over a short time span (200 ms). Although several methods including the solvothermal method and top-down lithography have been reported for polyelemental nanoparticle preparation,[16−20] the carbothermal shock heating method has several advantages including the ultrashort reaction time (200 ms) and the atomic-scale mixing of the polyelemental components.[21,22] In addition, the alloy nanoparticles achieved by the Joule heating method exhibit uniform particle size distribution without significant aggregation.

The overall fabrication scheme for preparing polyelemental catalysts is described in Figure 1a. We used a freestanding CNF film, which was produced by the electrospinning of polyacrylonitrile (PAN) polymer nanofiber and subsequent high-temperature pyrolysis, as a support for Joule heating. Indeed, CNF is the most widely used substrate in electrochemical applications because of its conductive and porous features, which provide a stable electrode structure during cycling.[23−25] The electrospun nanofibers comprising the CNF film with highly porous structures showed an average fiber

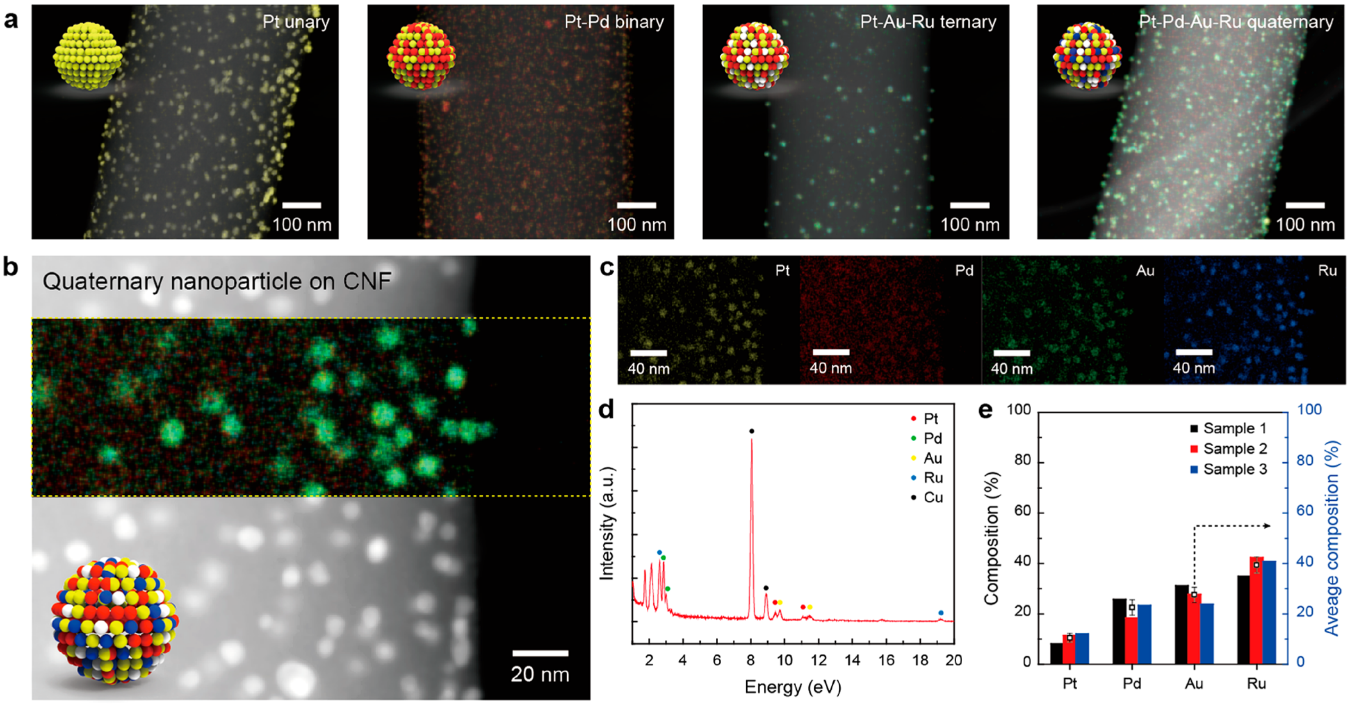

Figure 2. Characterization of quaternary nanoparticles synthesized by thermal shock method. (a) TEM-EDS mapping of unary, binary, ternary, and quaternary nanoparticles. (b) TEM-EDS mapping of Pt−Pd−Au−Ru quaternary nanoparticles and (c) that of each metal element. (d) EDS spectrum of quaternary nanoparticles (Pt, Pd, Au, and Ru) and TEM grid (Cu). (e) Composition of nanoparticles.

diameter of ~500 nm. In this work, we controlled the oxygen content in the CNF by changing the CNF annealing temperature. Because liquid metal moves and harvests oxygen on the carbon surface during heating time, well-dispersed alloy nanoparticles are well formed on CNFs after Joule heating (Figure S1). Precursor solutions with different polyelemental combinations were then prepared by dissolving four metal chlorides (H_2PtCl_6, $PdCl_2$, $HAuCl_4$, and $RuCl_3$) in ethanol (0.05 M) and were loaded on CNF film. We prepared the precursor solutions with 14 different combinations of Pt, Pd, Au, and Ru: single (Pt, Pd, Au, and Ru), binary (Pt−Pd, Pt−Ru, Pd−Au, Pd−Ru, and Au−Ru), ternary (Pt−Pd−Au, Pt−Pd−Ru, Pt−Au−Ru, and Pd−Au−Ru), and quaternary (Pt−Pd−Au−Ru) components. The solutions were then rapidly heated over a short time span (200 ms) by introducing the current momentarily. The temperature rose rapidly for a short time and then went down quickly, resulting in the formation of well-mixed polyelemental nanoparticles on CNF support.

A photographic image shows that temperature rose rapidly on the CNF substrates during the Joule heating over a short time (Figure 1b). When a current of 1 A flowed for 200 ms, the temperature rapidly rose and fell (see Movie 1 in the Supporting Information). Figure 1c shows SEM images of the cathode before and after Joule heating, confirming the homogeneous formation of polyelemental nanoparticles on CNF via Joule heating.

TEM observations further confirmed the formation of metal nanoparticles on the CNF (Figure 1d). Spherical nanoparticles were clearly visible on a single strand of CNF with a diameter of about 500 nm. Well-dispersed nanoparticles consisting of four noble metals (Pt−Pd−Au−Ru) had a relatively uniform size with a diameter of about 13 nm, as determined by averaging the TEM image measurements of approximately 200 nanoparticles. On an oxygen-rich carbon surface such as CNF film, metal nanoparticles could be well-distributed without any noticeable aggregation because carbon is consumed by the liquid metal, and the surface-bound residual oxygen during the Joule heating can be distributed across the oxygen sites. Notably, the size distribution (~12.9 ± 1.9 nm) of our polyelemental nanoparticles of for all 14 metal combinations is very uniform, exhibiting narrow standard deviation of 2 nm. In general, metal nanoparticles synthesized by the previous heating process have a wide size distribution because the aggregation of liquid metal at high temperatures easily occurs.

To verify that the catalysts with polyelemental components were homogeneously mixed, TEM and its corresponding EDS were conducted (Figure 2). Figure 2a shows representative TEM-EDS mapping images of single, binary, ternary, and quaternary polyelemental nanoparticles on CNF. Each combination was confirmed by EDS mapping and its spectrum (Figure S2). While we could detect only yellow (Pt) dots on the CNF in the first EDS mapping data, the binary, ternary, and quaternary nanoparticles showed mixed-colored nanoparticles with two (Pt, yellow; Pd, red), three (Pt, yellow; Pd, red; Ru, blue) and four (Pt, yellow; Pd, red; Au, green; Ru, blue;) metal elements. All nanoparticles had similar feature sizes of 11−15 nm diameter regardless of the polyelemental combination and composition. Therefore, the size effect of the polyelemental catalysts could be ruled out.

To further confirm the well-mixed formation of the polyelemental components, we analyzed the EDS-TEM mapping, line profile, and composition for a representative Pt−Pd−Au−Ru quaternary nanoparticle (Figure 2b−e). The four elements in the quaternary nanoparticles were well-mixed, confirming no significant separation of any specific elements throughout the data sets. First, in the partially overlapped TEM and EDS mapping images (Figure 2b), the elemental mapping images clearly reveal that the four metal components were

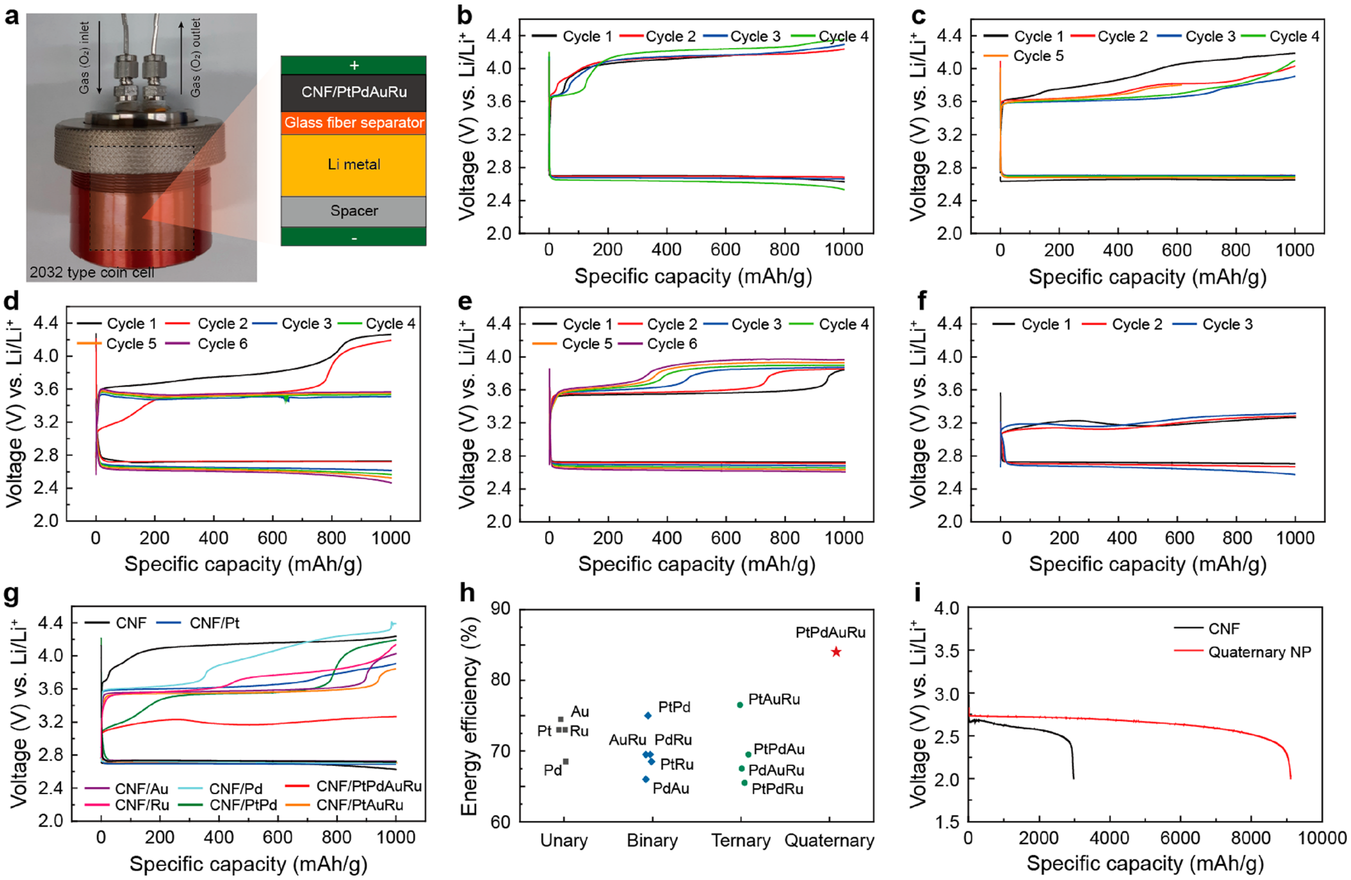

Figure 3. Li−O_2 battery performance of the electrode fabricated by Joule heating. (a) Li−O_2 single-cell device and its configuration. Charge−discharge curves of (b) CNF, (c) CNF/Pt, (d) CNF/Pt−Pd, (e) CNF/Pt−Au−Ru, (f) CNF/Pt−Pd−Au−Ru, and (g) all samples under 100 mA g^{-1} in a limited capacity of 1000 mAh g^{-1}. (h) Number of noble metals and the corresponding energy efficiency of the prepared electrode materials. (i) Full discharge curves of CNF and CNF/Pt−Pd−Au−Ru electrodes under 2.0 V cutoff condition at a current density of 100 mA g^{-1}.

well-mixed. Similar to the TEM image shown in Figure 1d, nanoparticles with a diameter of 13 nm showed mixed colors of four different metal elements (Pt-yellow, Pd-red, Au-green, and Ru-blue) at the same positions as shown in the mapping image, indicating that the four elements were well-mixed within a single nanoparticle. This can be confirmed by Figure 2c, the elemental EDS mapping result, which shows that there is also no difference in position. In the line profile (Figure S3) passing through the nanoparticle, the metal elements showed high counts in only one region where the nanoparticles were not separated. In addition, the four metal elements, Pt, Pd, Au, and Ru, were clearly detected in the EDS spectrum (Figure 2d). The large peak on the TEM grid was assigned to Cu. From the EDS spectra of several quaternary nanoparticles, the composition of the quaternary nanoparticle was calculated to be 10.5% Pt, 22.5% Pd, 27.6% Au, and 39.4% Ru (Figure 2e) when an equal ratio (1:1:1:1) of the four metal elements was loaded as a precursor solution. Furthermore, by changing the composition of the precursor solution, a quaternary nanoparticle with a different composition could be easily obtained (Figure S4); therefore, this system can be useful for comparing the catalytic activities of polyelemental nanoparticles with diverse composition.

Figure 3 and Figure S5 exhibit the Li−O_2 battery performances for cathodes containing 14 different combinations of polyelemental catalysts. The configuration of the Li−O_2 single-cell battery device is presented in Figure 3a. The Li−O_2 cell consisted of CNF with catalysts (cathode), glass fiber (separator), lithium metal (anode), and spacer. The Li−O_2 cells are fabricated by using CNFs cathode including various polyelemental catalysts and then assembled into a custom-designed container with O_2 gas flowing through the gas inlet and outlet. The Li−O_2 cells are evaluated at the limited capacity of 1000 mAh g^{-1} and a cutoff potential of 2.0 V under constant current application.. Figure 3b−f shows the charge−discharge curves of polyelemental catalysts in a limited capacity of 1 000 mAh g^{-1} under a current density of 100 mAh g^{-1}. To activate the surface, the cells were precycled until their electrochemical profiles were stabilized. As shown in Figure 3b, the CNF electrode without catalysts exhibited relatively high overpotential between the typical ORR plateau at around 2.7 V and the high OER potential at 4.1 V, resulting in an energy efficiency of 65%. For single catalyst-loaded CNFs, there were no significant changes in the ORR potential, but the OER potential decreased, showing increased energy efficiencies for Pt, Pd, Au, and Ru at 73, 68, 74, and 73%, respectively (Figures 3c and S5). The Li−O_2 cells with binary and ternary catalysts on CNFs also exhibited lower OER potentials than that of CNF with enhanced energy efficiencies for Pt−Pd, Pt−Ru, Pd−Au, Pd−Ru, and Au−Ru at 75, 69, 66, 70, and 70%, respectively (Figures 3d and S6) and for Pt−Pd−Au, Pt−Au−Ru, Pt−Au−Ru, and Pt−Pd−Ru at 70, 77, 66, and 68%, respectively (Figures 3e and S7). Although the CNFs with single, binary, and ternary catalysts showed better performance

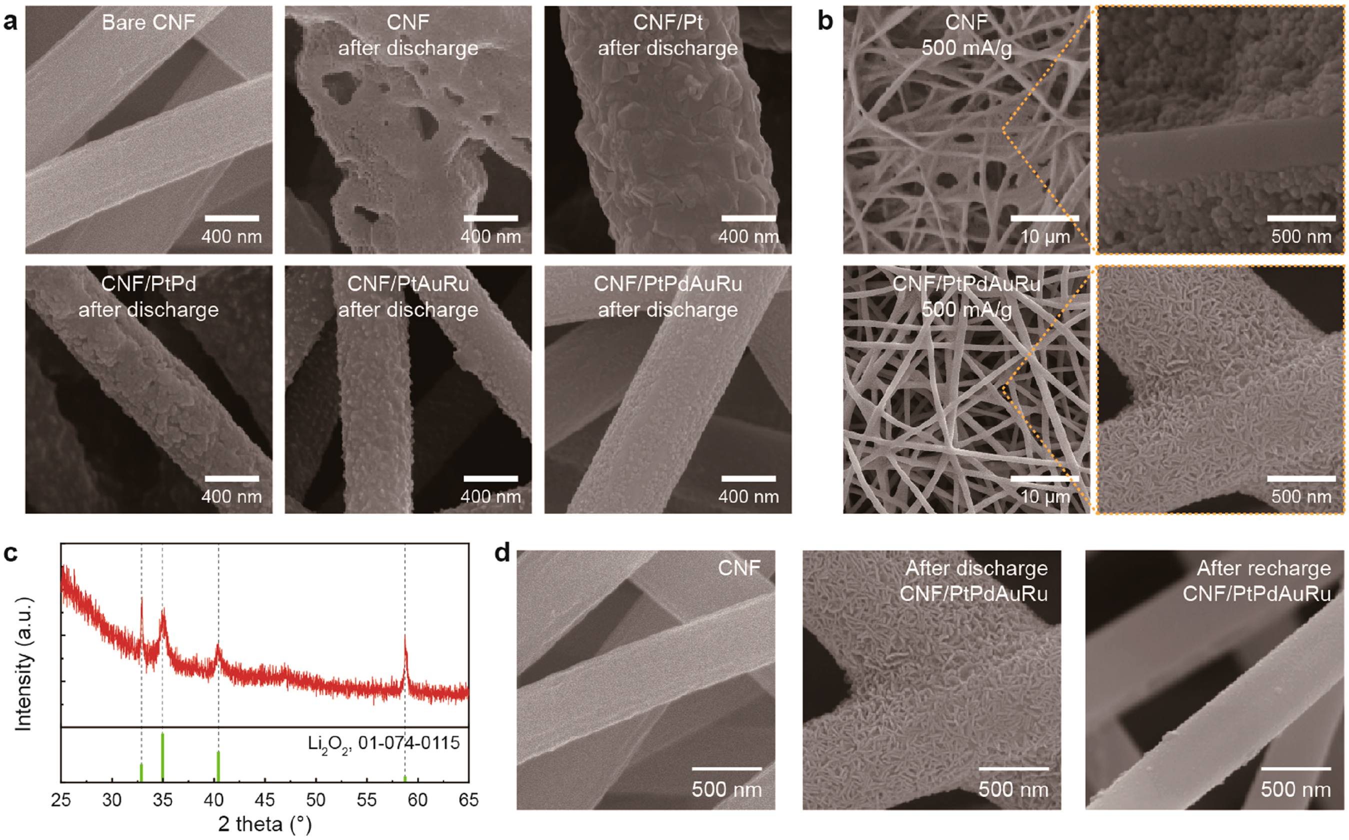

Figure 4. Morphological difference of the discharge product. (a) Pristine CNF and *ex situ* SEM images of the electrodes (CNF, CNF/Pt, CNF/Pt−Pd, CNF/Pt−Au−Ru, and CNF/Pt−Pd−Au−Ru) after discharge at 100 mA g^{-1} at a limited capacity of 1000 mAh g^{-1}. (b) *Ex situ* SEM images of the CNF and CNF/Pt−Pd−Au−Ru electrodes after discharge at 500 mA g^{-1} under a limited capacity of 1000 mAh g^{-1}. (c) *Ex situ* XRD pattern of the CNF/Pt−Pd−Au−Ru electrode after discharge. (d) SEM images of the CNF/Pt−Pd−Au−Ru electrode in pristine form, after discharge, and after recharge at 500 mA g^{-1}.

compared to pristine CNF, the deviations in the catalytic activities were not significantly changed with changing element numbers for all combinations except the quaternary combination. As an exemplar, the Pt−Pd−Au−Ru quaternary catalyst-loaded CNF (CNF/Pt−Pd−Au−Ru) electrode had a significantly reduced OER overpotential at around 3.2 V with markedly high energy efficiency of 84% (Figure 3f). The reaction potential of the irreversible formation of byproducts due to the carbon is above 3.5 V. Therefore, the low OER overpotential and the maintaned terminal voltage at charging of CNF/Pt−Pd−Au−Ru cathode can suppress the formation of byproducts during cycling.[26,27] Because the performance of the quaternary catalyst was much improved compared to those of the single, binary, and ternary catalysts, we concluded that Pt−Pd−Au−Ru is the most efficient catalyst among the single and polyelemental catalysts tested in the charge reaction.

The voltage profiles of CNF and the CNF with polyelemental catalysts are compared in Figure 3g, and their energy efficiencies are summarized in Figure 3h. Among the single catalysts, Pt, Pd, and Ru showed comparably high energy efficiencies of 73−74%. Among the binary catalysts, Pt−Pd exhibited the highest energy efficiency of 75%, while for ternary catalysts, Pt−Au−Ru had an efficiency of 76%. More importantly, the substantial energy efficiency enhancemet (84%) was observed in the quaternary catalyst, that is, Pt−Pd−Au−Ru. Thus, incorporating Pt in the polyelemental catalyst could improve the catalytic activity, and the Li−O_2 performance was the highest when all four elements were incorporated in the polyelemental catalyst.

Figure 3i shows the full discharge curves of CNF/Pt−Pd−Au−Ru electrodes under the 2.0 V cutoff condition at a current density of 100 mA g^{-1} (areal current density of 0.5 mA cm^{-2}). We considered the gravimetric energy density by evaluating the specific capacity calculated based on the total weight of the electrode including the catalyst. The discharge capacity of the CNF/Pt−Pd−Au−Ru electrode was 9130 mAh g^{-1} (45.65 mAh cm^{-2}), which was about three times higher than that (2960 mAh g^{-1} (14.8 mAh cm^{-2})) of the pristine CNF electrode. The CNF/Pt−Pd−Au−Ru electrode was binder-free, which was also advantageous in achieving high-energy-density Li−O_2 batteries.

To understand the electrochemical behavior in the polyelemental catalysts, we examined the surface morphology of the discharge products formed in the cells using the quaternary catalyst (Figure 4). Although the behavior of polyelemental catalysts is not fully understood, the enhanced Li−O_2 cell performance in the case of quaternary catalyst may be attributed to the increased O_2 adsorption energy. The Li_2O_2 morphology is significantly influenced by the adsorption/binding energy between O_2 and the cathode surface: the first step of the discharge process is the formation of O_2^-/LiO_2, which occurs either on the cathode surface or in the electrolyte solution in accordance with the adsorption/binding energy. Catalysts with strong O_2 affinity, such as noble metals, undergo electrochemical reduction on the cathode surface as the main

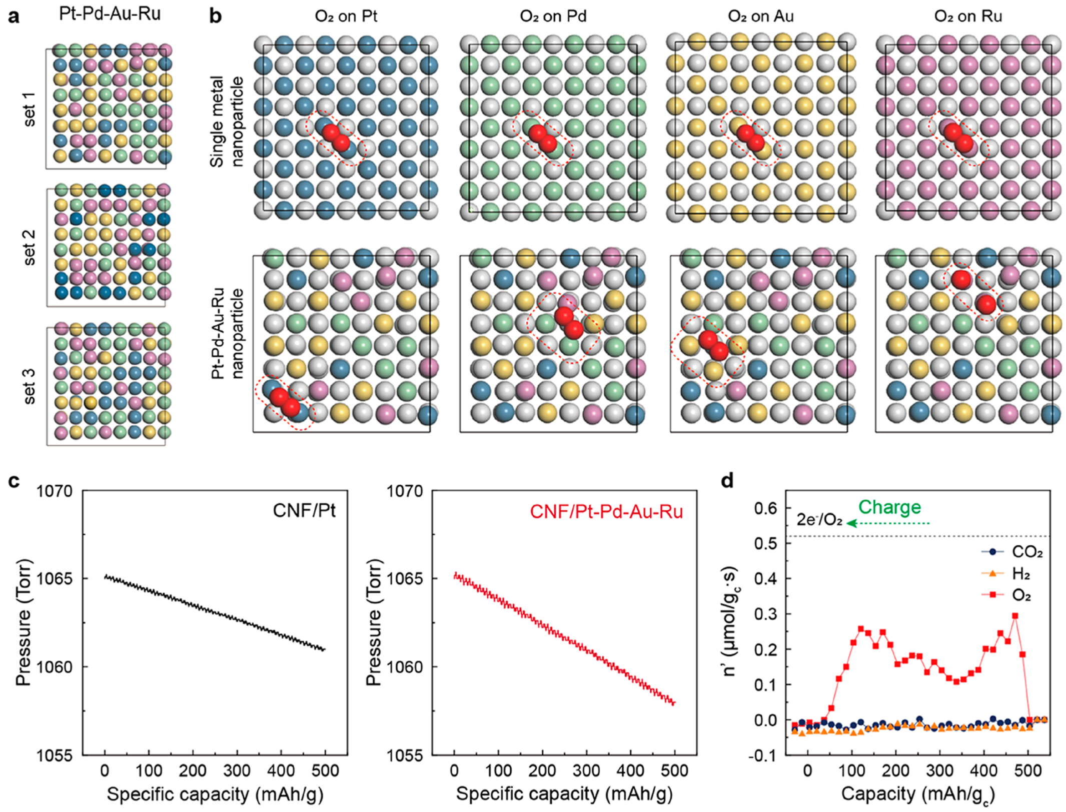

Figure 5. O_2 adsorption on the catalyst surface. (a) Configurations of Pt−Pd−Au−Ru, (b) relaxed configurations of O_2 on single-metal nanoparticles and the respective metals in Pt−Pd−Au−Ru nanoparticles, (c) pressure drop of O_2 gas during the discharge in the headspace of the cells using CNF/Pt and CNF/Pt−Pd−Au−Ru cathodes, and (d) O_2, CO_2, and H_2 evolution during the charging of the cell with the CNF/Pt−Pd−Au−Ru cathode.

Li_2O_2 formation step according to the equation $LiO_2 + e^- + Li^+ \rightarrow Li_2O_2$. Because of the rapid nucleation on the surface, the resultant Li_2O_2 has a small particle size or it is formd as a thin film. A cathode with weak O_2 affinity, such as CNF, results in Li_2O_2 formation in the electrolyte solution by the disproportionation pathway, according to the equation $LiO_2 + LiO_2 \rightarrow LiO_2 + O_2$, resulting in the large-sized Li_2O_2 formation.[28−30] Thus, the O_2 adsorption energy determines the Li_2O_2 morphology, which has a significant influence on the Li−O_2 cell performance.

As shown in Figure 4a, the discharge products of the CNF electrode were deposited in a thick, irregular, and aggregated form, with randomly distributed features on the CNF. These formations were likely due to the weak binding strength between O_2 and CNF, which led to the solution growth pathway of Li_2O_2. Unlike the CNF electrode, electrodes incorporating noble metals resulted in discharge products that were rather uniformly deposited on the surface of CNF due to the strong binding between O_2 and noble-metal-based catalysts. Notably, the discharge product of the CNF/Pt−Pd−Au−Ru electrode exhibited thin filmlike morphology. Unlike the pristine CNF, the discharged CNF/Pt−Pd−Au−Ru electrode exhibited width that grew from 400 to 630 nm because of the formation of thin filmlike deposits on the cathode, which demonstrates the strong O_2 adsorbability of the CNF/Pt−Pd−Au−Ru electrode. The controlling of Li_2O_2 particle size and shape is considered to be the most effective strategy in improving electrochemical performance due to the insulating nature of Li_2O_2. Thus, small-sized particles as well as ultrathin filmlike Li_2O_2 is recommended to improve the decomposition kinetics during charging. Moreover, the small-sized Li_2O_2 provides an improved interface between Li_2O_2 and the cathode surface, facilitating the OER due to the rapid electron transfer at the contact sites. The thin film morphology of the CNF/Pt−Pd−Au−Ru electrode also provides an indirect evidence of a large number of active sites for Li_2O_2 nucleation.

To further study the nucleation behavior of the CNF/Pt−Pd−Au−Ru electrodes, both of the CNF and CNF/Pt−Pd−Au−Ru electrodes were discharged with a higher current density of 500 mA g^{-1} (higher current density results in a higher nucleation rate). As presented in Figure 4b, the CNF electrode exhibited localized deposition of discharge products due to the weak O_2 adsorption; however, the particle size remained small compared with particles formed under lower current density because of the rapid charge transfer. Under the higher current density, the CNF/Pt−Pd−Au−Ru electrode showed a significant morphological transition from the thin film to wormlike particles. The resultant Li_2O_2 was delocalized on the electrode surface with a uniform size and minimal agglomeration which validate the high stability and the large number of active sites on the cathode surface. Thus, the excellent kinetics of the Pt−Pd−Au−Ru quaternary catalyst can be attributed to the strong O_2 adsorption strength and the large number of Li_2O_2 nucleation sites on the Pt−Pd−Au−Ru catalyst.

The reduced overpotential associated with the generation of small Li_2O_2 particles was also attributed to the surface graphene layer formed on the polyelemental catalysts. As characterized by TEM (Figure S8), the catalysts were covered

https://doi.org/10.1021/acsnano.0c06528
ACS Nano 2021, 15, 4235−4244

with a graphene layer. When a catalyst is not directly exposed but is encapsulated by a graphene layer, the π-electron density on the CNF surface increases, and the electron transfer on the surface interface is delocalized. Accordingly, the delocalized, small Li_2O_2 particles can lead to enhanced Li−O_2 battery performance.

We carried out X-ray diffraction (XRD) analysis on the CNF/Pt−Pd−Au−Ru cathode after full discharge. The main discharge product was Li_2O_2 with a small amount of Li_2CO_3 as a side product (Figure 4c). The morphologies of the fully discharged CNF and CNF/Pt−Pd−Au−Ru are compared in Figure S9, which shows that the CNF cathode exhibited randomly distributed Li_2O_2 with small-size deposits as well as large isolated particles, whereas the CNF/Pt−Pd−Au−Ru cathode showed uniformly distributed Li_2O_2 on the surface of the cathode. These results are consistent with those presented in Figure 4a,b. To prove that the discharge−charge reaction is reversible, an SEM image was taken after cell recharge; this revealed that the recharged morphology after complete decomposition of deposited Li_2O_2 particles was almost same as in the pristine state (Figure 4d). In addition, the CNF/Pt−Pd−Au−Ru electrode was cycled more than 20 times at a limited capacity of 1000 mAh g^{-1} at 500 mA g^{-1}, which also supports the reversibility of the Li−O_2 reaction.

To demonstrate the enhanced catalytic activity of the CNF/Pt−Pd−Au−Ru electrode more conclusively, a simulation study and *in situ* differential electrochemical mass spectroscopy (DEMS) analysis were conducted,with the results shown in Figure 5. As highlighted by Figure 4, the superior catalytic activity of the quaternary Pt−Pd−Au−Ru catalyst can be attributed to strong O_2 adsorption at the catalyst surface. To prove this, the O_2 adsorption energies corresponding to the single and quaternary Pt−Pd−Au−Ru catalysts were calculated and compared. Figure 5a shows three configurations of Pt−Pd−Au−Ru catalysts, which were created using the special quasi-random structure (SQS) method. The energies of sets 1, 2, and 3 are 745.0, −744.6, and −743.8 eV, respectively. Accordingly, set 1, which has the most stable configuration, was selected to calculate the O_2 adsorption energy. To compare the O_2 adsorption energy between single-element and Pt−Pd−Au−Ru nanoparticles, it was calculated when molecular oxygen was adsorbed in the top-bridge-top (tbt) configuration as this configuration was the most stable configuration when molecular oxygen was adsorbed on the nanoparticles. Figure 5b shows the relaxed configurations of O_2 on each metal of the Pt−Pd−Au−Ru catalyst and the single nanoparticles from the TBT configuration. The adsorption energy of Pt−Pd−Au−Ru was measured as −2.15, −5.34, −1.34, and −2.44 eV for Pt, Pd, Ru, and Au, respectively, resulting in an average adsorption energy of 2.82 eV. Additionally, the adsorption energy of single nanoparticles is −2.25, −3.41, −0.96, and −2.06 eV for Pt, Pd, Ru, and Au, respectively, corresponding to an average adsorption energy of 2.17 eV for single metals. Although the tbt configuration (Figure S10) is maintained in the final O_2 configurations of all single-element nanoparticles, only Pt preserves the tbt configuration in the quaternary case (bottom row of Figure 5b). In contrast, the molecular oxygen is dissociated for Ru and changes from the tbt configuration to facilitate adsorption with other metals for Pd and Au. The behavior of molecular oxygen in Pt−Pd−Au−Ru catalysts leads to stronger adsorption strength than observed for single nanoparticles. The average adsorption energy of Pt−Pd−Au−Ru increases by 0.62 eV compared to that of single-metal nanoparticles, meaning that the Pt−Pd−Au−Ru catalyst facilitates the adsorption of O_2 more effectively.

The strong O_2 adsorption on the CNF/Pt−Pd−Au−Ru cathode was demonstrated *via in situ* DEMS analysis (Figure 5c,d). Because the discharge product (Li_2O_2) can be generated according to the equations $O_2 + Li^+ + e^- \rightarrow LiO_2$ and $LiO_2 + e^- + Li^+ \rightarrow Li_2O_2$, the amount of O_2 that is consumed is a key parameter for determining the formation of Li_2O_2. The consumption of O_2 during cell discharge was measured quantitatively using *in situ* DEMS analysis, as shown in Figure S11. Given the volume of the cell headspace, the measured pressure change in the cells could be translated to the molar volume of gas using the ideal gas law. As shown in Figure 5c, during discharge the cell using the CNF/Pt−Pd−Au−Ru cathode consumed 2.95 μmol of O_2, representing far higher consumption than the CNF/Pt cathode, which consumed 2.39 μmol of O_2. On the basis of a comparison with the cathodic current, we can infer that the ratio between electrons and molecular oxygen (e^-/O_2) in the CNF/Pt−Pd−Au−Ru cathode during discharge to be approximately 1.90, which agrees closely with the theoretical value of 2.0 e^-/O_2. Through *in situ* DEMS analysis, we showed that the cell based on the CNF/Pt−Pd−Au−Ru cathode demonstrated high O_2 evolution during the charge process with the evolution of parasitic gas species such as CO_2 and H_2 kept to a minimum. These data indicate that the CNF/Pt−Pd−Au−Ru cathode exerts a strong catalytic effect in the reversible reaction of $Li^+ + 2e^- + O_2 \leftrightarrow Li_2O_2$ during discharge and charge processes in Li−O_2 cells. Thus, the strong adsorption of O_2 on the CNF/Pt−Pd−Au−Ru cathode during ORR and improved catalytic activity during OER was clearly demonstrated.

CONCLUSION

In summary, we investigated the effects of catalysts composed of Pt, Pd, Au, and Ru on the electrochemical performance of a Li−O_2 battery. Fourteen different combinations of well-mixed catalysts were prepared by Joule heating on carbon nanofibers. The electrochemical performances of the diverse combinations of polyelemental catalyst showed that Pt-containing polyelemental catalysts exhibit improved catalytic activity, and the deviations in the catalytic activities did not significantly change with changing element numbers for all combinations except the quaternary combination. The catalytic activity was substantially increased when four elements are incorporated within a single polyelemental catalyst. The CNF/Pt−Pd−Au−Ru quaternary nanoparticles exhibited a reduced overpotential at 0.45 V and a high discharge capacity based on the total cathode weight at 9,130 mAh g^{-1} due to the strong O_2 adsorbability. This quaternary nanoparticle exhibited two characteristics for Li−O_2 batteries: (1) During ultrafast Joule heating (200 ms), up to four metals could be well-mixed in a nanoparticle with a 13 nm diameter. (2) The CNFs including polyelemental catalyst exhibited superior Li−O_2 cell performance with reduced overpotential and increased discharge capacity. We expect the ultrafast Joule heating method can lead to further investigations on various catalyst combinations and compositions. This is a step toward finding an optimum alloy catalyst for Li−O_2 batteries.

METHODS

Preparation of Polyacrylonitrile (PAN) Nanofibers (NFs). To synthesize the polymeric ink solution, 1 g of polyacrylonitrile (PAN, 150 000 Mw, Sigma-Aldrich) was dissolved in 6.5 g of *N*,*N*-dimethylformamide (DMF, 99.8%, Sigma-Aldrich) with magnetic stirring (room temperature, 300 rpm). After the solution was homogeneously stirred at 70 °C for 3 h, the electrospinning process was implemented. The polymer solution was placed in a syringe with a metal nozzle (25 G), and a voltage of 15 kV was applied between the collector and the metal nozzle. The distance from the needle to the collector was 15 cm, and the feeding rate was 10 μL min^{-1}. After the electrospinning process, the freestanding PAN NF membrane that was attached to the collector was gently detached with tweezers. The freestanding PAN film was air-stabilized at 280 °C for 1 h. The stabilized PAN film was annealed at high temperatures (800, 850, and 900 °C) for 2 h with Ar purging (300 sccm). Annealed PAN films have different resistance depending on annealing temperature.

Joule Heating for Synthesis of Alloy Nanoparticles. For the Joule heating experiment, the annealed PAN film was cut into 2 mm × 20 mm pieces and then connected to a Cu electrode using silver paste. The metal precursor solution (50 mM) was prepared by dissolving each precursor (50/*n* mM, with *n* representing the number of metal elements) in ethanol. Ten microliters of the precursor solution was loaded on the film and dried in the oven (60 °C) for 30 min. The sample was placed in a customized vacuum chamber, and an external power source was connected to the Cu electrodes. Finally, a current pulse was applied to the sample for 200 ms under an Ar atmosphere.

Measurements. The surface of the electrodes was characterized using scanning electron microscopy (SEM, Tescan Mira 3 LMU FEG, 20 kV). The crystal structures of the discharged products of the electrode were confirmed by X-ray powder diffractometry (XRD, Rigaku Ultima IV diffractometer) using a graphite monochromator equipped with a Cu Kα line (40 kV/40 mA). The CNF and the polyelemental catalysts supported on the CNF were used as the cathode and were assembled in the Li−O_2 cells in an Ar-filled glovebox using 2032-type coin cells. A solution of 1 M lithium nitrate ($LiNO_3$, Sigma-Aldrich) in DMA (Sigma-Aldrich) was used as the electrolyte for the Li−O_2 cells. The water content was determined to be less than 30 ppm by Mettler-Toledo Karl Fischer titration. Li foil served as the anode. The mass loading of the cathode was 1.0−1.5 mg. Charge−discharge curves were obtained with a battery cycler (WBCS-3000, WonAtech) at applied current densities of 100 and 500 mA g^{-1} (areal current density of 0.5 and 2.5 mA cm^{-2}). The amount of consumed O_2 during discharge was analyzed by *in situ* differential electrochemical mass spectroscopy (DEMS) analysis. A pressure sensor (UNIK 5000, GE, pressure range, −1−7 bar; accuracy, ±0.1% full scale) was placed in line to measure the gas pressure change in the cell headspace. The cells were fed with high-purity O_2 gas (>99.999%), and the real-time pressure drop in the cells during discharge was monitored during the test.

Calculations. The quantum chemistry calculations were performed with the Vienna *ab Initio* Simulation Package (VASP)[31] with the projector augmented wave potentials.[32] For Pt, Pd, Au, Rh, single nanoparticleas were created by a 4 × 4 × 2 supercell of fcc structure and quaternary Pt−Pd−Au−Ru were generated using a special quasirandom structure (SQS) method.[33,34] The SQS method facilitates the generation of a minimally sized supercell that approximates a disordered system. The SQS method implemented in (ATAT)[35] is widely used for the polyelement system.[36,37] The quaternary Pt−Pd−Au−Ru was created with 4 × 4 × 2 supercells of fcc structure like single nanoparticles which consist of 4 layers and 128 atoms in a unit cell. By performing the SQS method three times, three configurations of quaternary Pt−Pd−Au−Ru were geometrically optimized in order to find the most energetically stable structure. The geometry optimization of single nanoparticles and quaternary Pt−Pd−Au−Ru was performed with the Perdue−Burke−Ernzerhof[38] of the generalized gradient approximations for exchange-correlation functional. *K*-point sampling was carried out using a 4 × 4 × 4 Monkhorst−Pack grid,[39] and the energy cutoff was set to 500 eV. From the optimized bulk system of four single nanoparticles and the most stable configuration of quaternary Pt−Pd−Au−Ru, surface unit cells were created with a 15 Å vacuum layer along the (001) plane direction. All surface unit cells were geometrically optimized under the condition where the two bottom layers were fixed. The *K*-points were sampled using a 4 × 4 × 1 Monkhorst−Pack grid, and the energy cutoff was set to 500 eV for all surface calculations. The adsorption strength of molecular O_2 was compared when each metal was between the single nanoparticles and the quaternary Pt−Pd−Au−Ru. For the single nanoparticles, the adsorption energy was calculated when O_2 adsorbs in top-bridge-top (tbt) configuration. Likewise, it was calculated when O_2 was adsorbed on the surface of the quaternary Pt−Pd−Au−Ru in the tbt configuration for each metal. The adsorption energy of O_2 was defined by

$$E_{\text{adsroption}} = E_{\text{substrate},O_2} - (E_{\text{substrate}} + E_{O_2})$$

where $E_{\text{substrate}}$ is the energy of single nanoparticle or quaternary Pt−Pd−Au−Ru, and E_{O_2} is the energy of molecular oxygen.

ASSOCIATED CONTENT

Supporting Information

The Supporting Information is available free of charge at https://pubs.acs.org/doi/10.1021/acsnano.0c06528.

Additional figures and text (PDF)

Movie showing a current of 1 A flowing for 200 ms where the temperature rapidly rose and fell (AVI)

AUTHOR INFORMATION

Corresponding Authors

Hee-Tae Jung − *Department of Chemical and Biomolecular Engineering (BK-21 Plus) and Institute for Nanocentury, Korea Advanced Institute of Science and Technology (KAIST), Yuseong-gu, Daejeon, 305-701, Korea;* orcid.org/0000-0002-5727-6732; Email: heetae@kaist.ac.kr

Mihye Wu − *Department of Chemical and Biomolecular Engineering (BK-21 Plus), Institute for Nanocentury, and Applied Science Research Institute, Korea Advanced Institute of Science and Technology (KAIST), Yuseong-gu, Daejeon, 305-701, Korea;* orcid.org/0000-0003-1068-906X; Email: wumihye@krict.re.kr

Authors

Woo-Bin Jung − *Department of Chemical and Biomolecular Engineering (BK-21 Plus) and Institute for Nanocentury, Korea Advanced Institute of Science and Technology (KAIST), Yuseong-gu, Daejeon, 305-701, Korea; School of Engineering and Applied Sciences, Harvard University, Cambridge, Massachusetts 02138, United States*

Hyunsoo Park − *Department of Chemical and Biomolecular Engineering (BK-21 Plus), Korea Advanced Institute of Science and Technology (KAIST), Yuseong-gu, Daejeon, 305-701, Korea*

Ji-Soo Jang − *Applied Science Research Institute, Korea Advanced Institute of Science and Technology (KAIST), Yuseong-gu, Daejeon, 305-701, Korea; Department of Chemical and Environmental Engineering, Yale University, New Haven, Connecticut 06520-8286, United States;* orcid.org/0000-0001-6018-7231

Do Youb Kim − *Advanced Materials Division, Korea Research Institute of Chemical Technology, Yuseong-gu, Daejeon 34114, Korea;* orcid.org/0000-0002-0398-9075

Dong Wook Kim − *Advanced Materials Division, Korea Research Institute of Chemical Technology, Yuseong-gu, Daejeon 34114, Korea*

Eunsoo Lim − *Chemical Analysis Center, Korea Research Institute of Chemical Technology, Yuseong-gu, Daejeon 34114, Korea;* orcid.org/0000-0002-5193-7704

Ju Ye Kim − *Department of Chemical and Biomolecular Engineering (BK-21 Plus) and Institute for Nanocentury, Korea Advanced Institute of Science and Technology (KAIST), Yuseong-gu, Daejeon, 305-701, Korea;* orcid.org/0000-0003-4262-0569

Sungho Choi − *Advanced Materials Division, Korea Research Institute of Chemical Technology, Yuseong-gu, Daejeon 34114, Korea;* orcid.org/0000-0002-9834-4543

Jungdon Suk − *Advanced Materials Division, Korea Research Institute of Chemical Technology, Yuseong-gu, Daejeon 34114, Korea*

Yongku Kang − *Advanced Materials Division, Korea Research Institute of Chemical Technology, Yuseong-gu, Daejeon 34114, Korea; Department of Chemical Convergence Materials, University of Science and Technology (UST), Yuseong-gu, Dajeon 34113, Korea;* orcid.org/0000-0003-2898-872X

Il-Doo Kim − *Department of Materials Science and Engineering, Korea Advanced Institute of Science and Technology (KAIST), Yuseong-gu, Daejeon, 305-701, Korea;* orcid.org/0000-0002-9970-2218

Jihan Kim − *Department of Chemical and Biomolecular Engineering (BK-21 Plus), Korea Advanced Institute of Science and Technology (KAIST), Yuseong-gu, Daejeon, 305-701, Korea;* orcid.org/0000-0002-3844-8789

Complete contact information is available at:
https://pubs.acs.org/10.1021/acsnano.0c06528

Notes

The authors declare no competing financial interest.

ACKNOWLEDGMENTS

This research was supported by the National Research Foundation of Korea (NRF) grant funded by the Ministry of Science, ICT, and future Planning, Korea (MSIP, No. 2018R1A2B3008658 and No. 2019M3D1A2104100). This research was also supported by a grant from the Korea Research Institute of Chemical Technology (SS2122-20), Republic of Korea.

REFERENCES

(1) Bruce, P. G.; Freunberger, S. A.; Hardwick, L. J.; Tarascon, J. M. Li-O_2 and Li-S Batteries with High Energy Storage. *Nat. Mater.* **2012**, *11* (1), 19−29.

(2) Zhou, W.; Zhang, H.; Nie, H.; Ma, Y.; Zhang, Y.; Zhang, H. Hierarchical Micron-Sized Mesoporous/Macroporous Graphene with Well-Tuned Surface Oxygen Chemistry for High Capacity and Cycling Stability Li-O_2 Battery. *ACS Appl. Mater. Interfaces* **2015**, *7* (5), 3389−3397.

(3) Débart, A.; Bao, J.; Armstrong, G.; Bruce, P. G. An O_2 Cathode for Rechargeable Lithium Batteries: The Effect of a Catalyst. *J. Power Sources* **2007**, *174* (2), 1177−1182.

(4) Debart, A.; Paterson, A. J.; Bao, J.; Bruce, P. G. Alpha-MnO_2 Nanowires: A Catalyst for the O_2 Electrode in Rechargeable Lithium Batteries. *Angew. Chem., Int. Ed.* **2008**, *47* (24), 4521−4524.

(5) Ogasawara, T.; Debart, A.; Holzapfel, M.; Novak, P.; Bruce, P. G. Rechargeable Li_2O_2 Electrode for Lithium Batteries. *J. Am. Chem. Soc.* **2006**, *128*, 1390−1393.

(6) Li, F.; Zhang, T.; Zhou, H. Challenges of Non-Aqueous Li-O_2 Batteries: Electrolytes, Catalysts, and Anodes. *Energy Environ. Sci.* **2013**, *6*, 1125−1141.

(7) Black, R.; Adams, B.; Nazar, L. F. Non-Aqueous and Hybrid Li-O_2 Batteries. *Adv. Energy Mater.* **2012**, *2*, 801−815.

(8) Lee, J.-H.; Black, R.; Popov, G.; Pomerantseva, E.; Nan, F.; Botton, G. A.; Nazar, L. F. The Role of Vacancies and Defects in $Na_{0.44}MnO_2$ Nanowire Catalysts for Lithium-Oxygen Batteries. *Energy Environ. Sci.* **2012**, *5*, 9558−9565.

(9) Li, Y.; Wang, J.; Li, X.; Geng, D.; Banis, M. N.; Li, R.; Sun, X. Nitrogen-Doped Graphene Nanosheets as Cathode Materials with Excellent Electrocatalytic Activity for High Capacity Lithium-Oxygen Batteries. *Electrochem. Commun.* **2012**, *18*, 12−15.

(10) Chawla, N.; Chamaani, A.; Safa, M.; El-Zahab, B. Palladium-Filled Carbon Nanotubes Cathode for Improved Electrolyte Stability and Cyclability Performance of Li-O_2 Batteries. *J. Electrochem. Soc.* **2017**, *164* (1), A6303−A6307.

(11) Lu, Y.-C.; Gasteiger, H. A.; Parent, M. C.; Chiloyan, V.; Shao-Horn, Y. The Influence of Catalysts on Discharge and Charge Voltages of Rechargeable Li-Oxygen Batteries. *Electrochem. Solid-State Lett.* **2010**, *13*, A69−A72.

(12) Lu, Y.-C.; Xu, Z.; Gasteiger, H. A.; Chen, S.; Hamad-Schifferli, K.; Shao-Horn, Y. Platinum-Gold Nanoparticles: A Highly Active Bifunctional Electrocatalyst for Rechargeable Lithium-Air Batteries. *J. Am. Chem. Soc.* **2010**, *132*, 12170−12171.

(13) Antolini, E. Iridium as Catalyst and Cocatalyst for Oxygen Evolution/Reduction in Acidic Polymer Electrolyte Membrane Electrolyzers and Fuel Cells. *ACS Catal.* **2014**, *4* (5), 1426−1440.

(14) Kim, H.-J.; Jung, S. C.; Han, Y.-K.; Oh, S. H. An Atomic-Level Strategy for the Design of a Low Overpotential Catalyst for Li-O_2 Batteries. *Nano Energy* **2015**, *13*, 679−686.

(15) Cui, Z.; Li, L.; Manthiram, A.; Goodenough, J. B. Enhanced Cycling Stability of Hybrid Li-Air Batteries Enabled by Ordered Pd_3Fe Intermetallic Electrocatalyst. *J. Am. Chem. Soc.* **2015**, *137* (23), 7278−7281.

(16) Jung, W. B.; Jang, S.; Cho, S. Y.; Jeon, H. J.; Jung, H. T. Recent Progress in Simple and Cost-Effective Top-Down Lithography for Approximately 10 nm Scale Nanopatterns: From Edge Lithography to Secondary Sputtering Lithography. *Adv. Mater.* **2020**, *32* (35), No. e1907101.

(17) Berahim, N.; Basirun, W.; Leo, B.; Johan, M. Synthesis of Bimetallic Gold-Silver (Au-Ag) Nanoparticles for the Catalytic Reduction of 4-Nitrophenol to 4-Aminophenol. *Catalysts* **2018**, *8* (10), 412.

(18) Zhang, C.; Jiang, S. Z.; Yang, C.; Li, C. H.; Huo, Y. Y.; Liu, X. Y.; Liu, A. H.; Wei, Q.; Gao, S. S.; Gao, X. G.; Man, B. Y. Gold@Silver Bimetal Nanoparticles/Pyramidal Silicon 3D Substrate with High Reproducibility for High-Performance SERS. *Sci. Rep.* **2016**, *6*, 25243.

(19) Chen, P.-C.; Liu, X.; Hedrick, J. L.; Xie, Z.; Wang, S.; Lin, Q.-Y.; Hersam, M. C.; Dravid, V. P.; Mirkin, C. A. Polyelemental Libraries. *Science* **2016**, *352* (6293), 1565−1569.

(20) Chen, P. C.; Liu, G.; Zhou, Y.; Brown, K. A.; Chernyak, N.; Hedrick, J. L.; He, S.; Xie, Z.; Lin, Q. Y.; Dravid, V. P.; O'Neill-Slawecki, S. A.; Mirkin, C. A. Tip-Directed Synthesis of Multimetallic Nanoparticles. *J. Am. Chem. Soc.* **2015**, *137* (28), 9167−9173.

(21) Yao, Y.; Huang, Z.; Xie, P.; Lacey, S. D.; Jacob, R. J.; Xie, H.; Chen, F.; Nie, A.; Pu, T.; Rehwoldt, M.; Yu, D.; Zachariah, M. R.; Wang, C.; Shahbazian-Yassar, R.; Li, J.; Hu, L. Carbothermal Shock Synthesis of High Entropy Alloy Nanoparticlees. *Science* **2018**, *359*, 1489−1494.

(22) Lacey, S. D.; Dong, Q.; Huang, Z.; Luo, J.; Xie, H.; Lin, Z.; Kirsch, D. J.; Vattipalli, V.; Povinelli, C.; Fan, W.; Shahbazian-Yassar, R.; Wang, D.; Hu, L. Stable Multimetallic Nanoparticles for Oxygen Electrocatalysis. *Nano Lett.* **2019**, *19* (8), 5149−5158.

(23) Wu, Y.; Reddy, M. V.; Chowdari, B. V.; Ramakrishna, S. Long-Term Cycling Studies on Electrospun Carbon Nanofibers as Anode Material for Lithium Ion Batteries. *ACS Appl. Mater. Interfaces* **2013**, *5* (22), 12175−12184.

(24) Liu, D.; Zhang, X.; You, T. Electrochemical Performance of Electrospun Free-Standing Nitrogen-Doped Carbon Nanofibers and Their Application for Glucose Biosensing. *ACS Appl. Mater. Interfaces* **2014**, *6* (9), 6275−6280.

(25) Liu, M.; Zhang, P.; Qu, Z.; Yan, Y.; Lai, C.; Liu, T.; Zhang, S. Conductive Carbon Nanofiber Interpenetrated Graphene Architecture for Ultra-Stable Sodium Ion Battery. *Nat. Commun.* **2019**, *10* (1), 3917.

(26) Lim, H. D.; Song, H.; Kim, J.; Gwon, H.; Bae, Y.; Park, K. Y.; Hong, J.; Kim, H.; Kim, T.; Kim, Y. H.; Lepro, X.; Ovalle-Robles, R.; Baughman, R. H.; Kang, K. Superior Rechargeability and Efficiency of Lithium-Oxygen Batteries: Hierarchical Air Electrode Architecture Combined with a Soluble Catalyst. *Angew. Chem., Int. Ed.* **2014**, *53* (15), 3926−31.

(27) Ottakam Thotiyl, M. M.; Freunberger, S. A.; Peng, Z.; Bruce, P. G. The Carbon Electrode in Nonaqueous Li-O_2 Cells. *J. Am. Chem. Soc.* **2013**, *135* (1), 494−500.

(28) Lyu, Z.; Yang, L.; Luan, Y.; Renshaw Wang, X.; Wang, L.; Hu, Z.; Lu, J.; Xiao, S.; Zhang, F.; Wang, X.; Huo, F.; Huang, W.; Hu, Z.; Chen, W. Effect of Oxygen Adsorbability on the Control of Li_2O_2 Growth in Li-O_2 Batteries: Implications for Cathode Catalyst Design. *Nano Energy* **2017**, *36*, 68−75.

(29) Lyu, Z.; Zhou, Y.; Dai, W.; Cui, X.; Lai, M.; Wang, L.; Huo, F.; Huang, W.; Hu, Z.; Chen, W. Recent Advances in Understanding of the Mechanism and Control of Li_2O_2 Formation in Aprotic Li-O_2 Batteries. *Chem. Soc. Rev.* **2017**, *46* (19), 6046−6072.

(30) Wu, M.; Kim, D. Y.; Park, H.; Cho, K. M.; Kim, J. Y.; Kim, S. J.; Choi, S.; Kang, Y.; Kim, J.; Jung, H.-T. Formation of Toroidal Li_2O_2 in Non-Aqueous Li-O_2 Batteries with Mo_2CT_x MXene/CNT Composite. *RSC Adv.* **2019**, *9* (70), 41120−41125.

(31) Kresse, G.; Furthmüller, J. Efficient Iterative Schemes for *ab initio* Total-Energy Caculations Using a Plane-Wave Basis Set. *Phys. Rev. B: Condens. Matter Mater. Phys.* **1996**, *54*, 11169−11186.

(32) Blöchl, P. E. Projector Augmented-Wave Method. *Phys. Rev. B: Condens. Matter Mater. Phys.* **1994**, *50* (24), 17953−17979.

(33) Wei, S.; Ferreira, L. G.; Bernard, J. E.; Zunger, A. Electronic Properties of Random Alloys: Special Quasirandom Structures. *Phys. Rev. B: Condens. Matter Mater. Phys.* **1990**, *42* (15), 9622−9649.

(34) Zunger, A.; Wei, S.; Ferreira, L. G.; Bernard, J. E. Special Quasirandom Structures. *Phys. Rev. Lett.* **1990**, *65* (3), 353−356.

(35) van de Walle, A.; Asta, M.; Ceder, G. The Alloy Theoretic Automated Toolkit: A User Guide. *CALPHAD: Comput. Coupling Phase Diagrams Thermochem.* **2002**, *26*, 539−553.

(36) Zaddach, A. J.; Niu, C.; Koch, C. C.; Irving, D. L. Mechanical Properties and Stacking Fault Energies of NiFeCrCoMn High-Entropy Alloy. *JOM* **2013**, *65* (12), 1780−1789.

(37) Osei-Agyemang, E.; Balasubramanian, G. Surface Oxidation Mechanism of a Refractory High-Entropy Alloy. *NPJ. Mater. Degrad.* **2019**, *3* (1), 20.

(38) Perdew, J. P.; Burke, K.; Ernzerhof, M. Generalized Gradient Approximation Made Simple. *Phys. Rev. Lett.* **1996**, *77*, 3865−3868.

(39) Monkhorst, H. J.; Pack, J. D. Special Points for Brillouin-Zone Integrations. *Phys. Rev. B* **1976**, *13* (12), 5188−5192.

NOTE ADDED AFTER ASAP PUBLICATION

Published ASAP on March 11, 2021; Revised March 23, 2021 to correct spelling of author name (S.C.).